

Supplements to: Dissolved Mn(III) is a key redox intermediate in sediments of a seasonally euxinic coastal basin

S1. Description of the fieldwork campaigns performed in 2021

Sampling of the sediment at Scharendijke basin was performed during 8 sampling campaigns with RV *Navicula* each month from March to October 2021, following the same methods used in the fieldwork campaigns in 2020 presented in this study. An additional sampling event in August / September 2021 is reported in Żygadłowska et al. (2024a, b). These results are not included here, because we focus on the monthly output of the reactive transport model. During each campaign, a sediment core was collected using a UWITEC corer with a transparent PVC core liner (120 cm length, 6 cm inner diameter) to collect samples for NH_4^+ , alkalinity, SO_4^{2-} , H_2S , TD Fe, TD Mn and during four campaigns, for the determination of Mn oxide and Mn carbonate. The core was sectioned at a 1 cm resolution under a N_2 environment, the sections were subsequently centrifuged to separate the pore water from the solid phase. The supernatant was filtered over 0.45 μm pore size filters. Samples for the analysis of NH_4^+ were stored at -20°C and later analyzed using the indophenol blue method (Solórzano, 1968). The samples for alkalinity and SO_4^{2-} were stored at 4°C until analysis. Alkalinity was measured through titration with 0.01 M HCl, within 24 h after sampling and SO_4^{2-} was measured using ion chromatography (Metrohm 930 Compact IC Flex; detection limit for SO_4^{2-} of 50 $\mu\text{mol L}^{-1}$). The samples for H_2S analysis were diluted five times in a 2% Zn-acetate solution in a glass vial and stored at 4°C . These samples were analyzed using the phenylenediamine and ferric chloride method (Cline, 1969). Samples for TD Fe and Mn were acidified with 10 μL 35% suprapure HCl per ml of sample and stored at 4°C . These samples were analyzed via ICP-OES (Perkin Elmer Avio; detection limit 0.1 $\mu\text{mol L}^{-1}$ and 0.03 $\mu\text{mol L}^{-1}$ for Fe and Mn respectively). Samples for the analysis of the sediment residues were stored in N_2 -purged aluminum bags at -20°C . Later, the samples were freeze-dried and ground with an agate mortar and pestle under a N_2 environment. Solid phase speciation of Mn was then determined using a sequential extraction procedure as described in Lenstra et al. (2021).

S2. Detailed model description

The reactions in the model describe organic matter (OM) degradation involving a range of electron acceptors combined with secondary reactions of the reaction products (Table S5). Degradation of OM is facilitated, in successive order, by reduction of O_2 , NO_3^- , MnO_2 , $\text{Fe}(\text{OH})_3$ and SO_4^{2-} and finally OM is degraded via methanogenesis (Table S2; Froelich et al., 1979; Reed et al., 2011a; Rooze et al., 2016). Monod kinetics are used to describe the sequence of electron acceptors in OM degradation (Boudreau, 1997). In Monod kinetics, the oxidant with the highest metabolic free energy yield is used preferentially, until this species becomes limiting and the next oxidant in the sequence is used preferentially (Boudreau, 1996; Van Cappellen & Wang, 1996). The OM is assumed to include carbon (C), nitrogen (N) and phosphorus (P) in a ratio of C:N:P = 106:15.45:1 (based on Egger et al., 2016b). Hence, the rate of OM degradation in the sediment is directly linked to the NH_4^+ profiles. In the model,

reduction of MnO₂ can be coupled to oxidation of OM, Fe(II), H₂S and CH₄ (Table S2). Reduction of MnO₂ by OM, Fe(II) and H₂S is modeled as one electron transfer steps with Mn(III) as the product (Madison et al., 2013). Reduction of MnO₂ by CH₄ is modeled as a two electron transfer with Mn(II) as a product, because, to our knowledge, the one electron transfer step that is theoretically possible has never been demonstrated. Reduction of MnO₂ with NH₄⁺ as discussed by Hulth et al. (1999) and Thamdrup and Dalsgaard (2000) is not incorporated in the model, because the quantitative importance of this reaction is not well known. Reduction of dMn(III)-L is assumed to occur with Fe(II), H₂S and OM to form Mn(II), while oxidation of Mn(III) is assumed to occur with O₂ to form MnO₂. Reduction of dMn(III)-L by NO₂⁻ as described by Karolewski et al. (2021) is not incorporated in the model. Production of NO₂⁻ in the anoxic sediment is unlikely and concentrations in September are below the detection limit. Oxidation of Mn(II) with O₂ and precipitation as MnCO₃ removes Mn(II). Dissolved inorganic carbon in the model is the sum of carbon in HCO₃²⁻ and CO₂, which are produced or consumed in reactions. The dominant effect of adsorption of dissolved Mn(II) to solid phase Mn is related to transport through bioturbation (Slomp et al., 1997). At sites with little or no bioturbation, as is the case here, the effect of Mn(II) adsorption on modeled pore water profiles will be limited.

Depending on whether a compound is a solid or solute, its generic mass conservation is described by Eq. S1 or Eq. S2, respectively.

$$(1 - \varphi) \frac{\partial C_s}{\partial t} = -(1 - \varphi)v \frac{\partial C_s}{\partial z} + \sum R_s \quad (S1)$$

$$\varphi \frac{\partial C_{aq}}{\partial t} = \varphi D' \frac{\partial^2 C_{aq}}{\partial z^2} - \varphi u \frac{\partial C_{aq}}{\partial z} + \sum R_{aq} \quad (S2)$$

In these equations, φ is the sediment porosity, t is time (yr), C_s and C_{aq} are the concentrations of the solid and dissolved species (mol L⁻¹), respectively, D' is the diffusion coefficient of dissolved species in the porous medium (cm² yr⁻¹), z is the distance from the Sediment-Water Interface (SWI; cm), v and u (cm yr⁻¹) are advective velocities of solids and dissolved species, respectively and $\sum R_s$ and $\sum R_{aq}$ are net rates of chemical reactions of solid and dissolved species, respectively.

For porosity, a depth-dependent function is used to account for sediment compaction (Meysman et al., 2005; Reed 2011a; eq S3):

$$\varphi(z) = \varphi_\infty + (\varphi_0 - \varphi_\infty)e^{-\frac{y}{z}} \quad (S3)$$

In this equation, φ_0 is the porosity at the SWI, φ_∞ is the porosity at depth and y is the porosity attenuation factor/e-folding distance (Table S5).

In the last 20 years of the model run, the seasonal cycle of oxic – euxinic conditions was simulated by varying the bottom water O₂ and H₂S concentration, the influx of Fe oxides, Mn oxides, Mn carbonates and OM and the sedimentation rate (Fig.

S3). The boundary conditions for the bottom water concentration of O₂ were based on monitoring by Rijkswaterstaat (Directorate-General for Public Works and Water Management of the Netherlands) as reported in Żygadłowska et al. (2023a). The bottom water H₂S was varied together with O₂ and was either 0, or the concentration measured in the bottom water in September (111.8 µmol L⁻¹). Input of metal oxides was varied together with O₂ and was fitted to the sediment profiles. The input of Mn carbonates was also varied to fit the sediment profiles, because authigenic Mn carbonate formation alone was insufficient to induce the observed oscillations. OM input was varied to fit the sediment profiles. The input of OM and the sedimentation rate in April differ from those in the other oxic months, because the effect of a spring bloom was simulated. Such variations in OM input are in line with variations in primary productivity and OM supply from the North Sea known for this system (Hagens et al., 2015). Sedimentation rates for the model run until 2016 (4 years before the end of the model run) were based on Egger et al. (2016; 13.3 cm yr⁻¹). Between 60 – 80 cm depth, which is around where the shift in sedimentation rates is assumed, a shift in the oscillations is visible in for example the C_{org} and Mn oxides sediment profiles (Fig. 4). This shift is modeled by varying the input of these compounds through the seasons. For the last 4 years the sedimentation rate was set to 20 cm yr⁻¹, based on the onset of the shallowest peak in C_{org} at 20 cm depth (Fig. 4), which marks the C_{org} deposition of the previous year (i.e. spring 2019).

S3. Figures

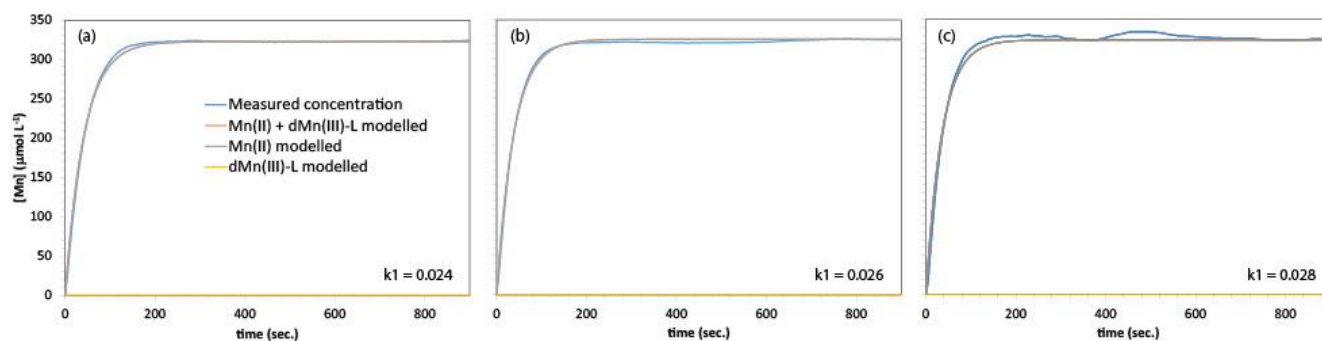


Figure S1: Kinetic curves (triplicates) that were used to determine the k_1 value for the kinetic reaction of Mn(II) at this site. In the lower right corner of the graph, the k_1 values are indicated.

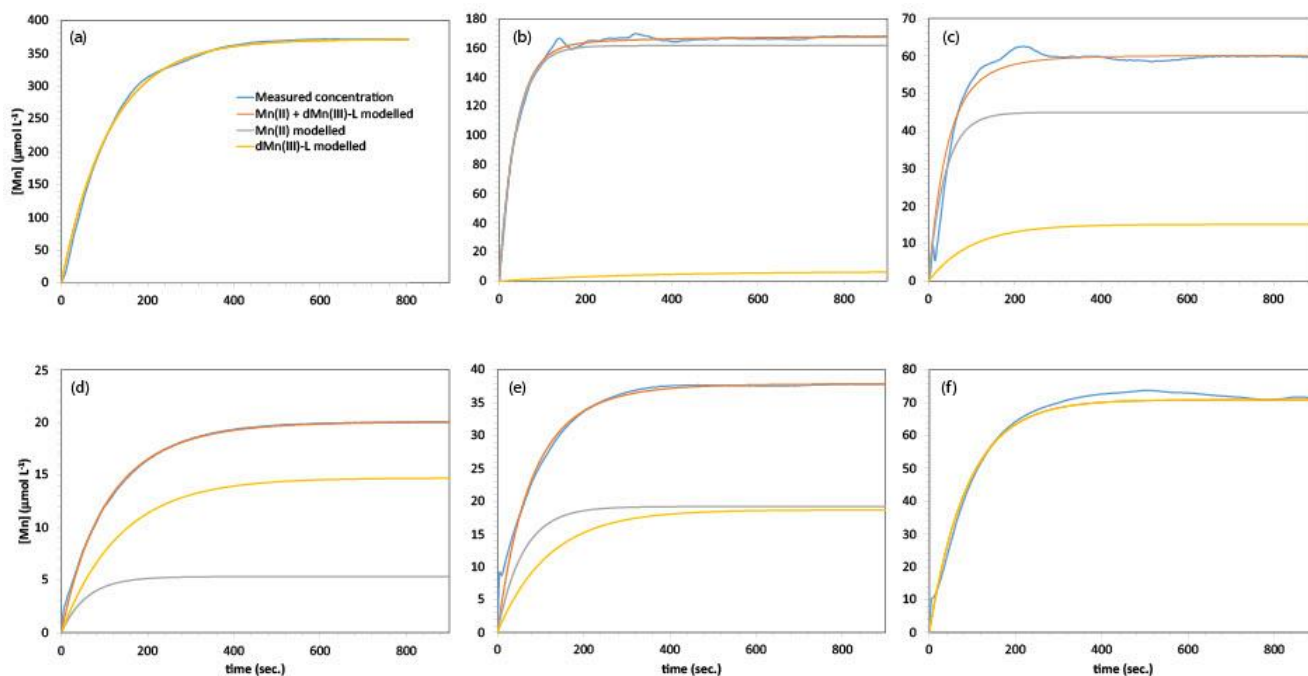


Figure S2, Kinetic curves that were measured and modeled Mn(II) and dMn(III)-L concentrations used to determine the Mn(II) and dMn(III)-L content of the samples from (a) 0 – 1 cm; (b) 6 – 7 cm; (c) 43 – 44 cm in March 2020 and (d) 1 – 2 cm; (e) 7 – 8 cm; (f) 23 – 24 cm in September 2020.

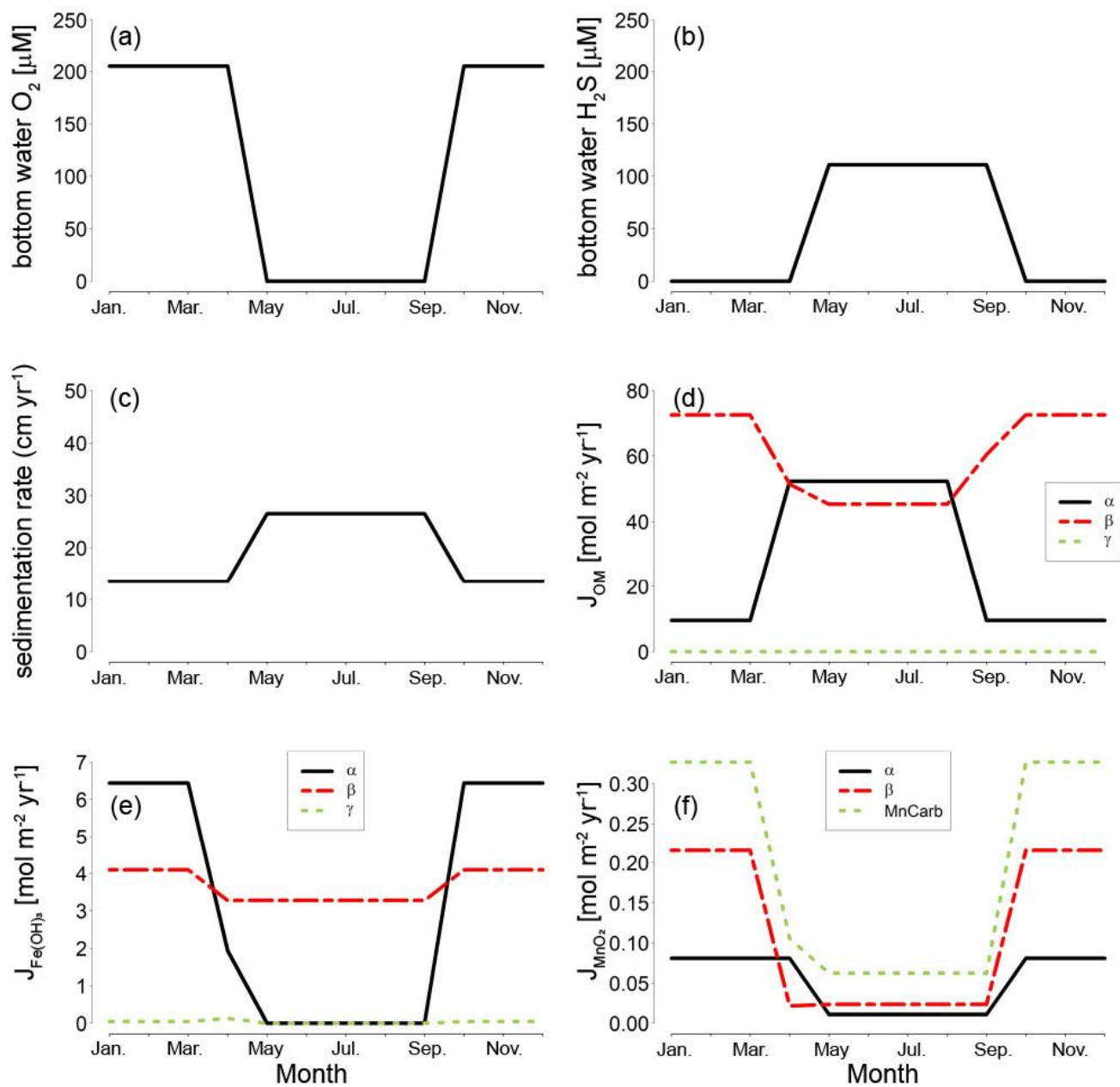


Figure S3. Seasonal variation in bottom water O_2 and H_2S , sedimentation rate, and in the flux of Fe oxides ($J_{Fe(OH)_3}$), flux of Mn oxides (J_{MnO_2}) and flux of organic matter (J_{OM}) at the sediment-water interface in the final year of the model simulations.

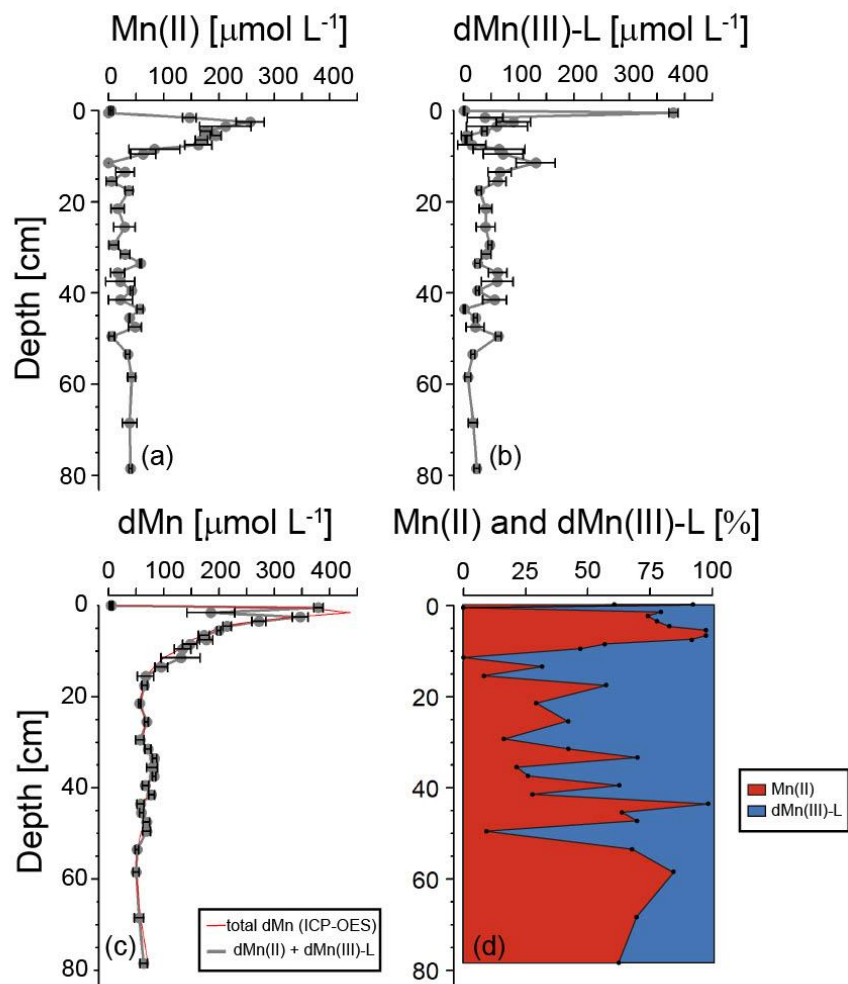
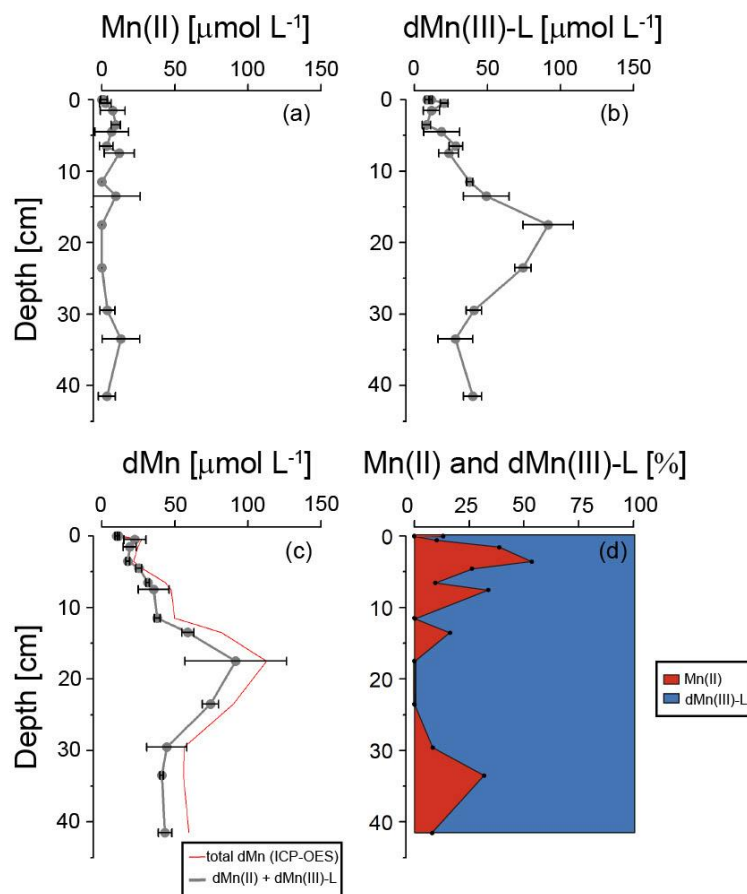


Figure S4: (a), (b) Data collected through spectrophotometric analysis of Mn(II) and dMn(III)-L in March, including error bars showing standard deviation (n=3). (c) The sum of Mn(II) and dMn(III)-L measured spectrophotometrically, including error bars showing standard deviation (n=3), compared with the total dissolved Mn measured with ICP-OES. (d) The contribution of Mn(II) and dMn(III)-L to the total dissolved Mn pool (determined as the sum of Mn(II) and dMn(III)-L) as percentage.



95 **Figure S5:** (a), (b) Data collected during the spectrophotometric analysis of Mn(II) and dMn(III)-L in September, including error bars showing standard deviation ($n = 3$). (c) The sum of Mn(II) and dMn(III)-L measured during the spectrophotometric method including error bars ($n = 3$), compared with the total dissolved Mn measured with ICP-OES. (d) The contribution of Mn(II) and dMn(III)-L to the total dissolved Mn pool (determined as the sum of Mn(II) and dMn(III)-L) as a percentage.

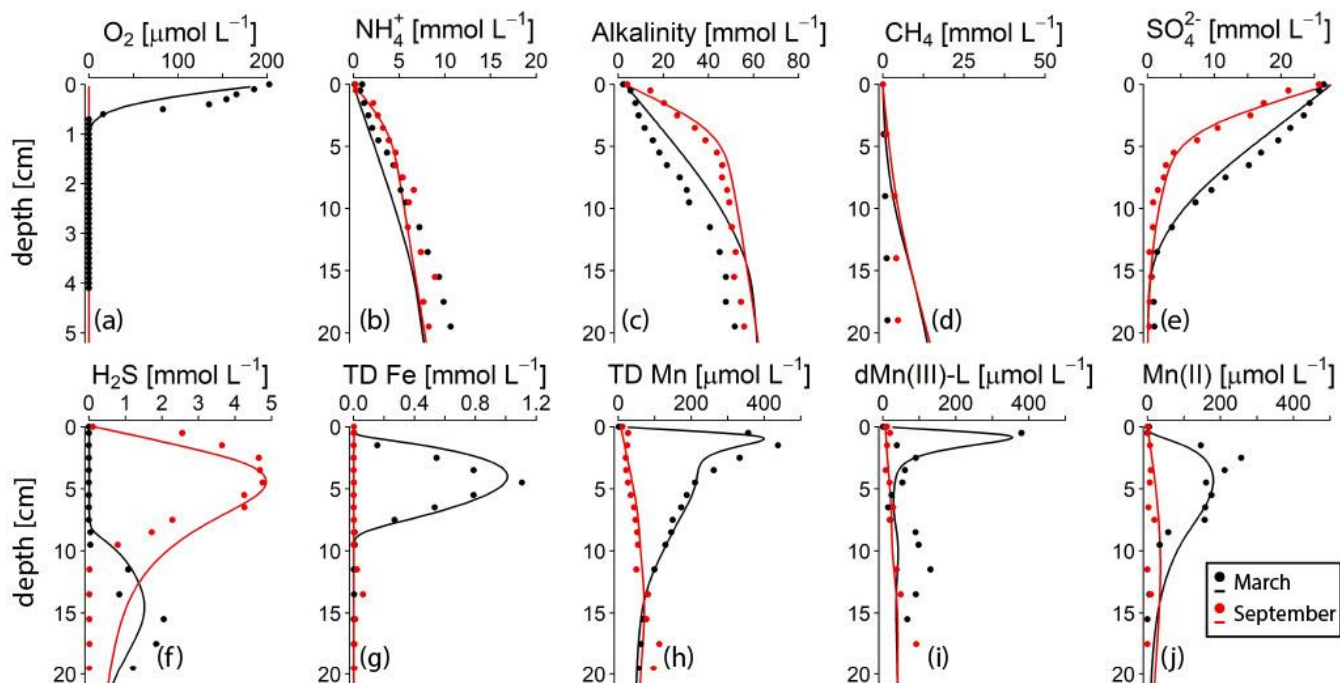


Figure S6. Top 20 cm of the pore water profiles of key components in March (black) and September (red) 2020. The dots represent measured concentrations, the lines indicate the results of the reactive transport model. Note the different depth scale on the y-axis for O₂. TD Fe and TD Mn refer to total dissolved Fe and total dissolved Mn. Profiles of Mn(II) and dMn(III)-L with standard deviation error bars (n =3) and the contribution to TD Mn (in %) can be found in Fig. S2, S3. No O₂ was detected in the sediment in September 2020 (Żygadłowska et al. 2023).

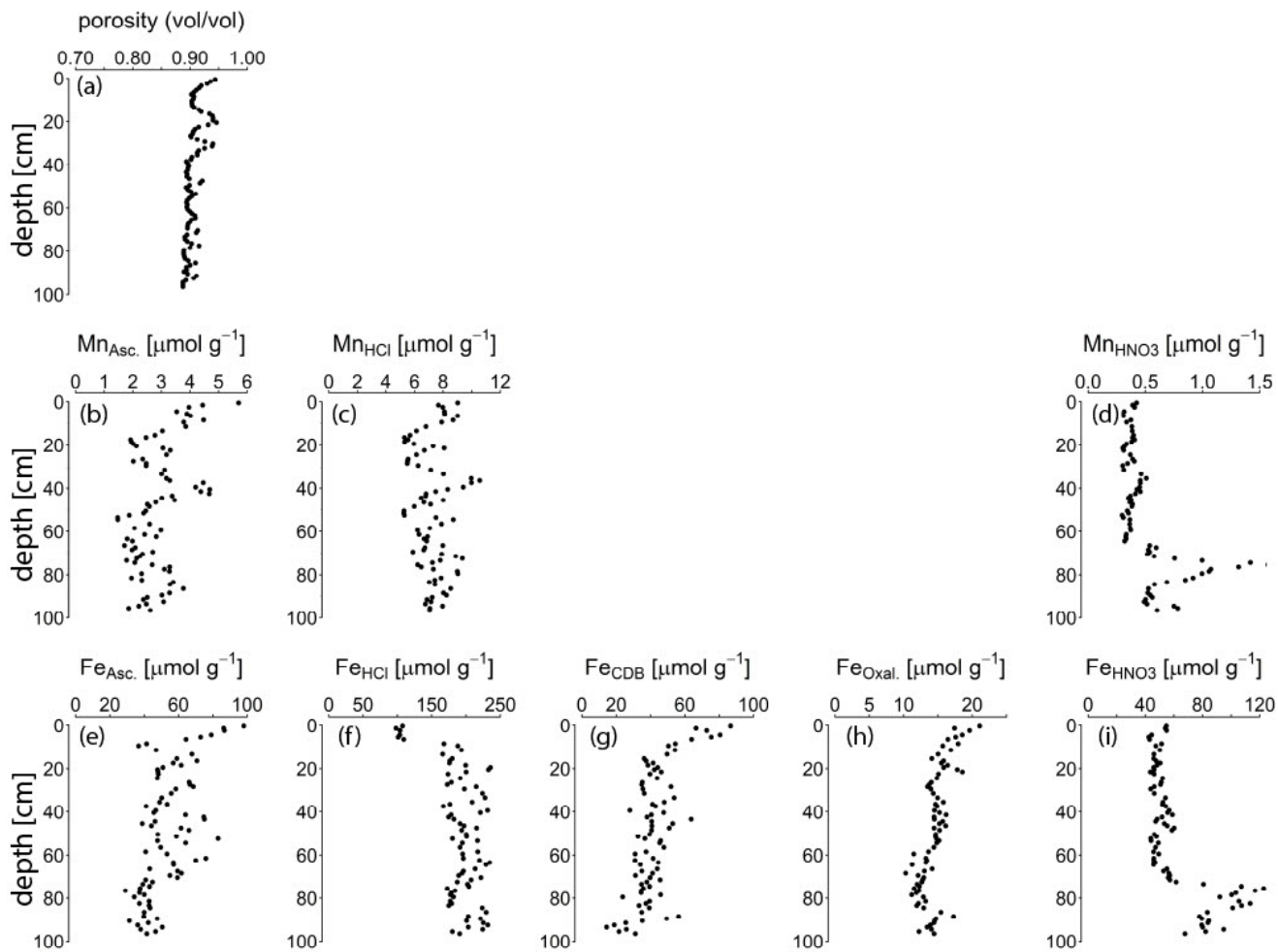
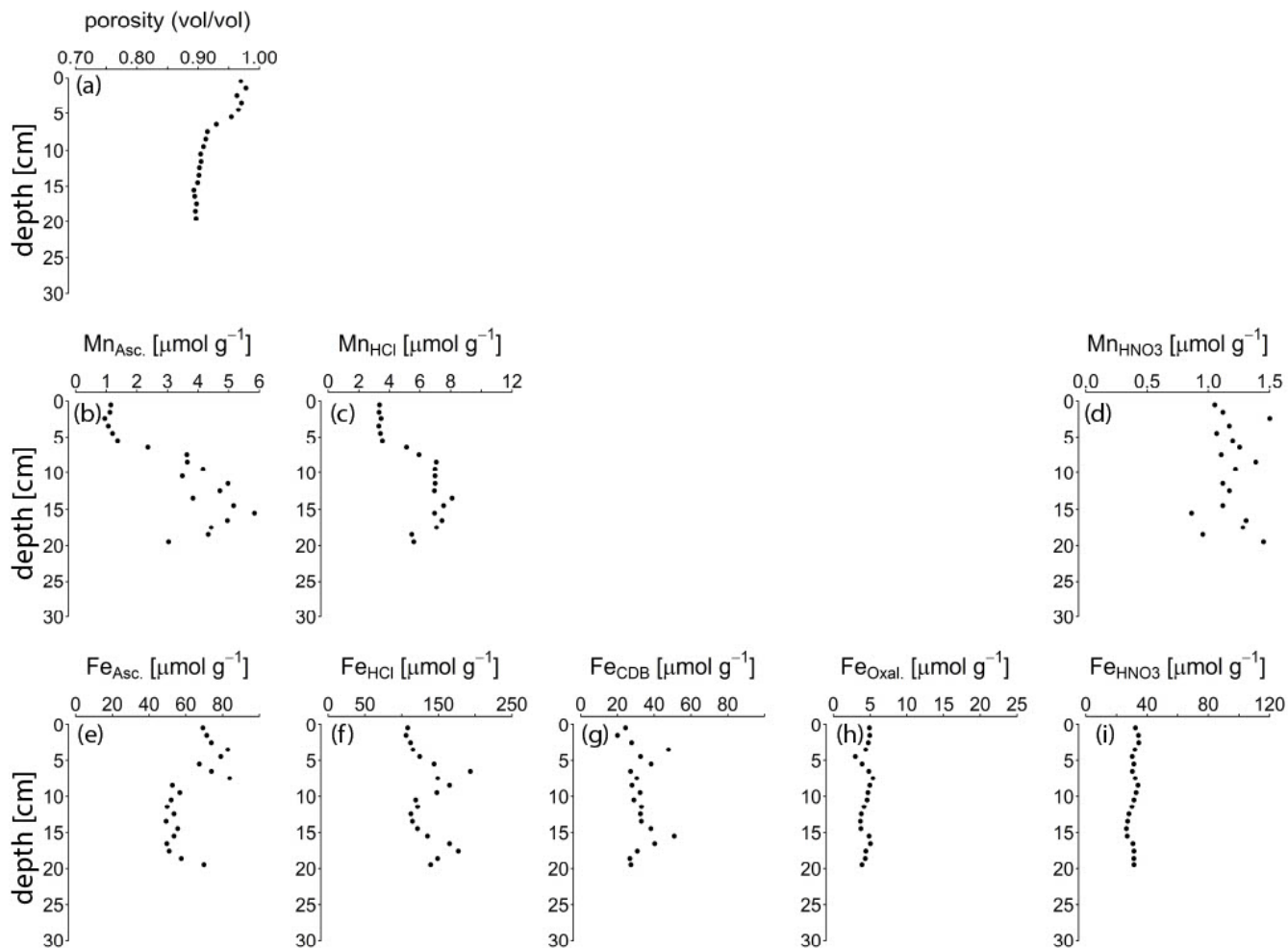


Figure S7: Porosity and all Mn and Fe fractions as determined in the sequential extraction, for the sediment collected in March 2020.



110

Figure S8: Porosity and all fractions extracted for Mn and Fe in the sequential extraction, for the sediment collected in September 2020 (0-20 cm).

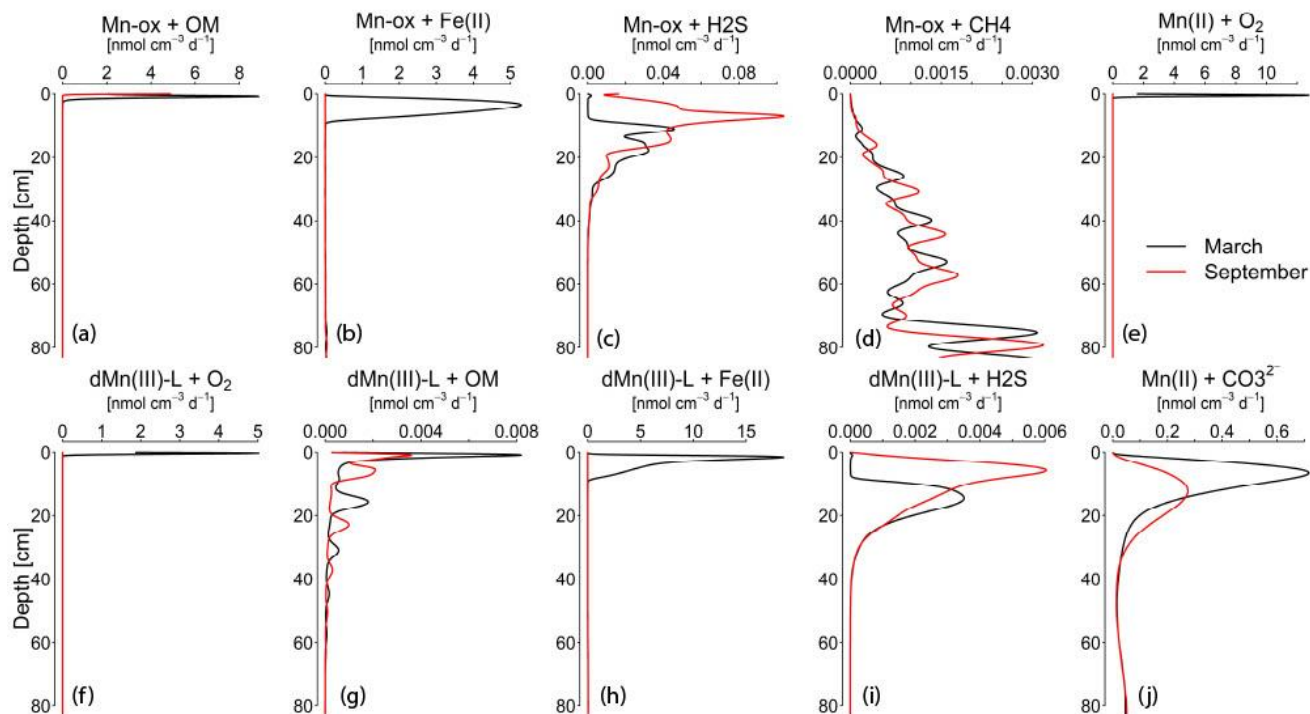


Figure S9: Depth profiles of the reaction rates, which form the basis for the rate integrations shown in Fig. 4.

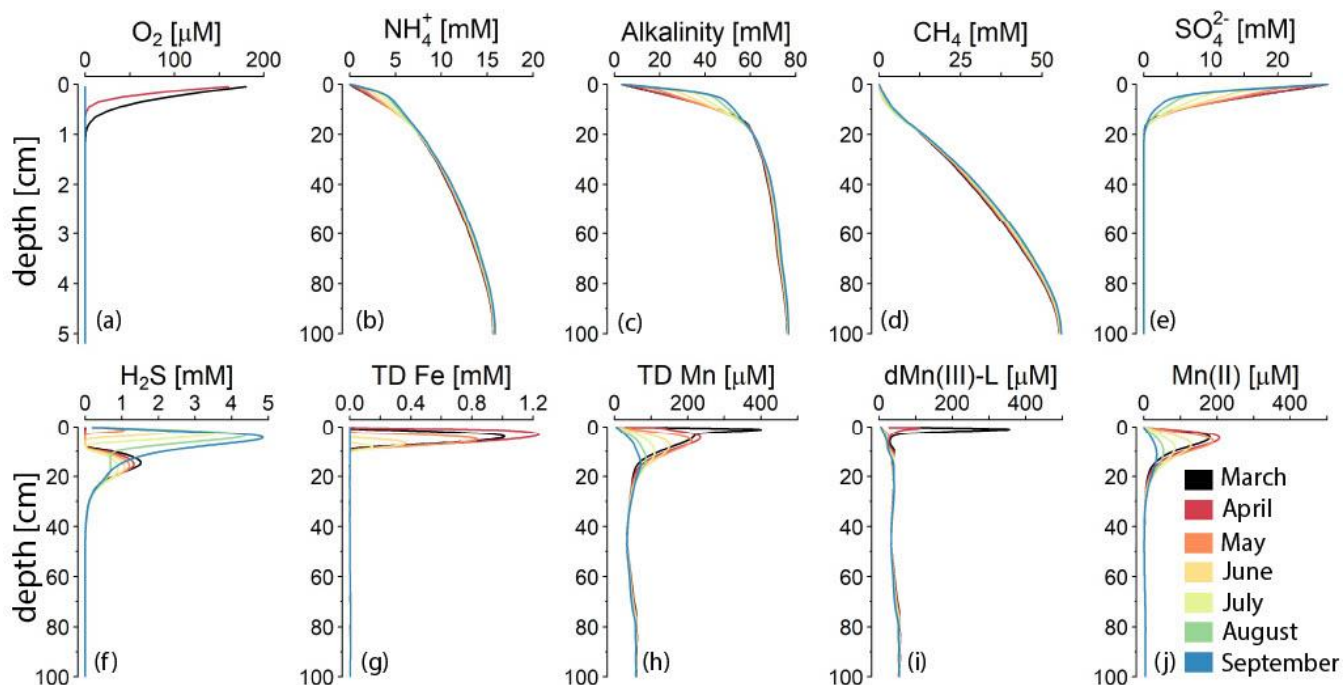
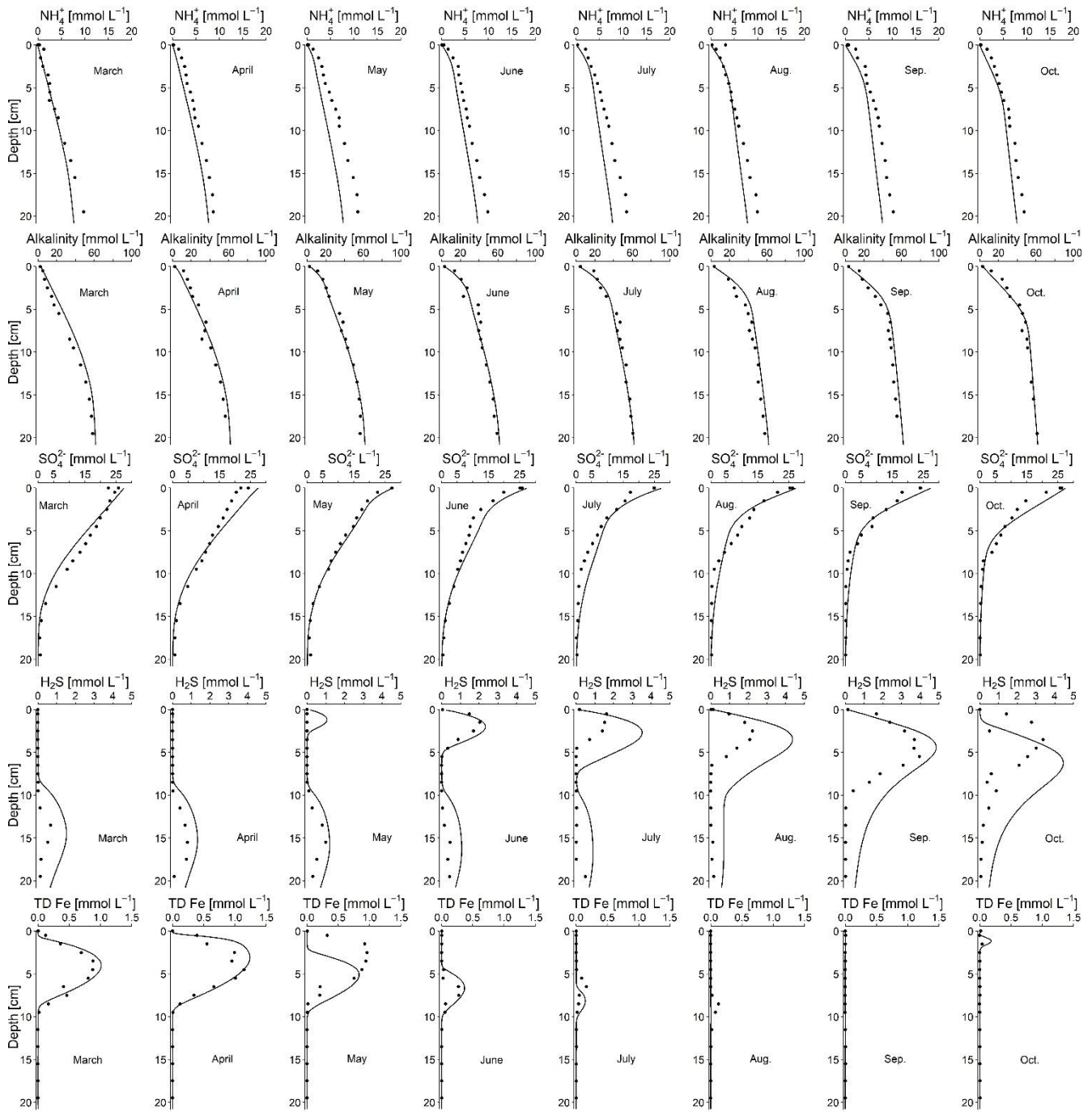
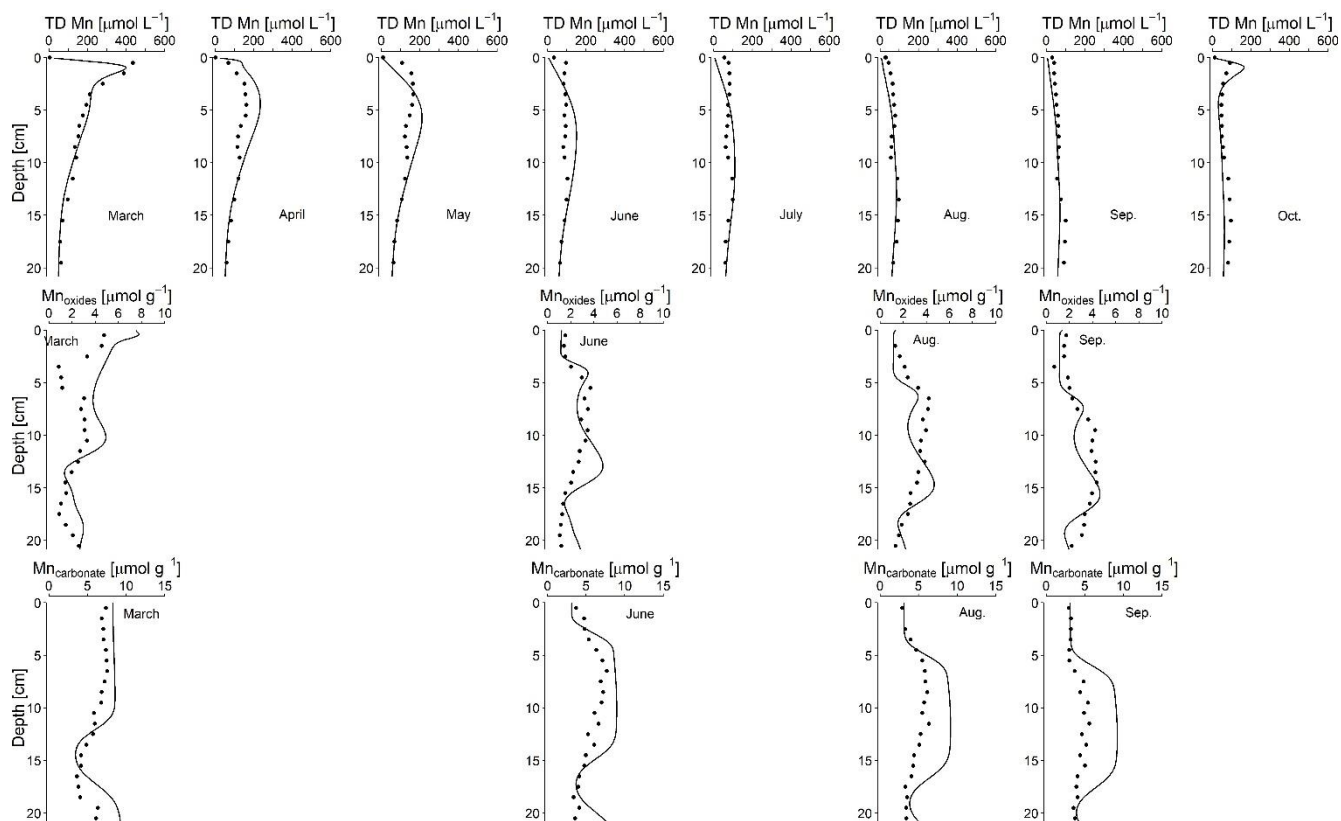


Figure S10. The change in pore water profiles between March and September when anoxic conditions develop in the basin. With the reactive transport model, pore water profiles can be extrapolated to months where no fieldwork was done in 2020.



120

Figure S11: Forward simulation of the reactive transport model to NH_4^+ , alkalinity, SO_4^{2-} , H_2S , TD Fe, TD Mn and, for 4 months, Mn oxides and Mn carbonates obtained during 8 sampling campaigns performed between March and October 2021. In 2021, Scharendijke experienced euxinia from June until September (Żygadłowska et al., 2024a). Part of this dataset was previously published in Żygadłowska et al. (2024a, b). The figure continues on the next page.



125

Continuation of figure S11.

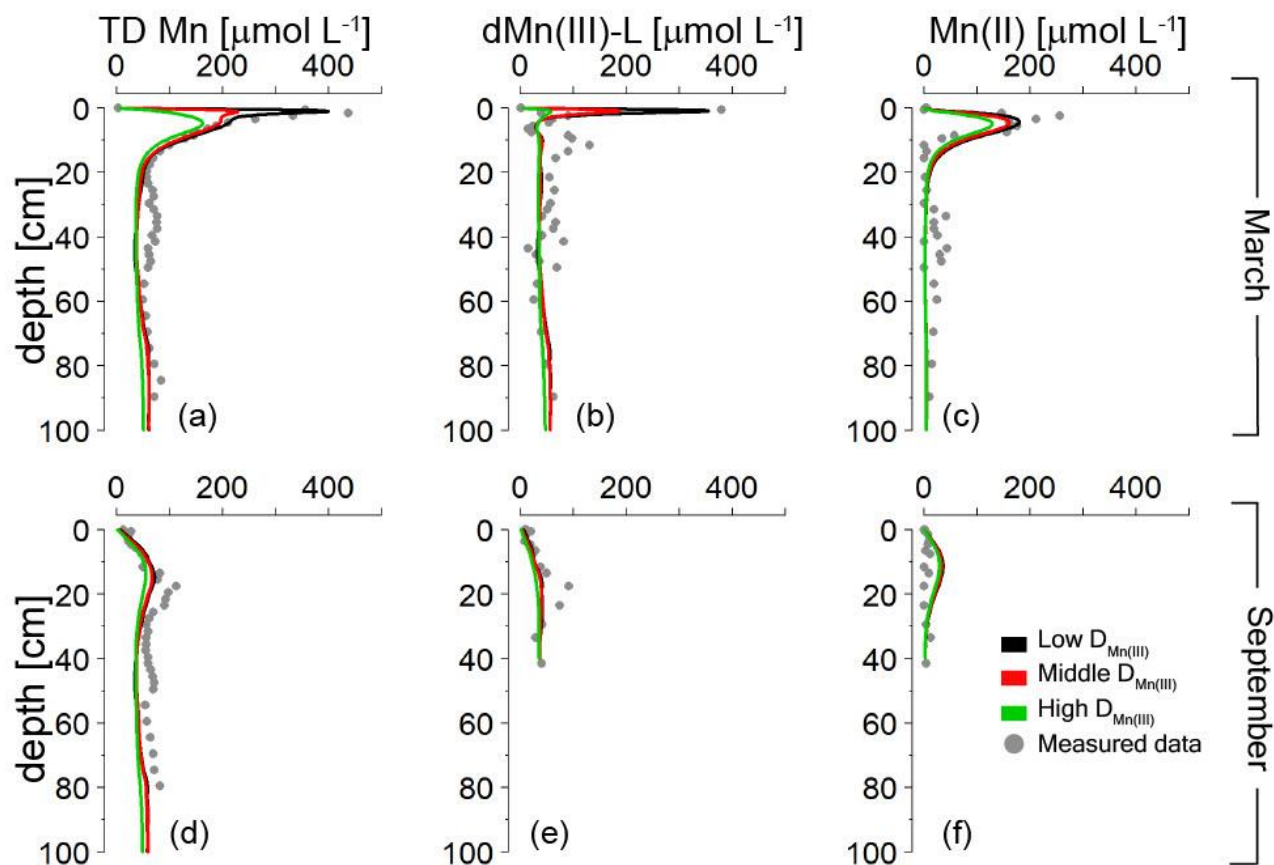


Figure S12: Model runs with different diffusion coefficients for dissolved Mn(III). The diffusion coefficients used and the range of diffusion coefficients for dissolved organic matter given in literature can be found in Table S6. When the diffusion coefficient decreases, the peak of dissolved Mn(III)-L and total dissolved Mn near the sediment-water interface in March is no longer well described by the model. The diffusion coefficient does not have a large effect on the pore water profiles of Mn(II) and dMn(III)-L in September.

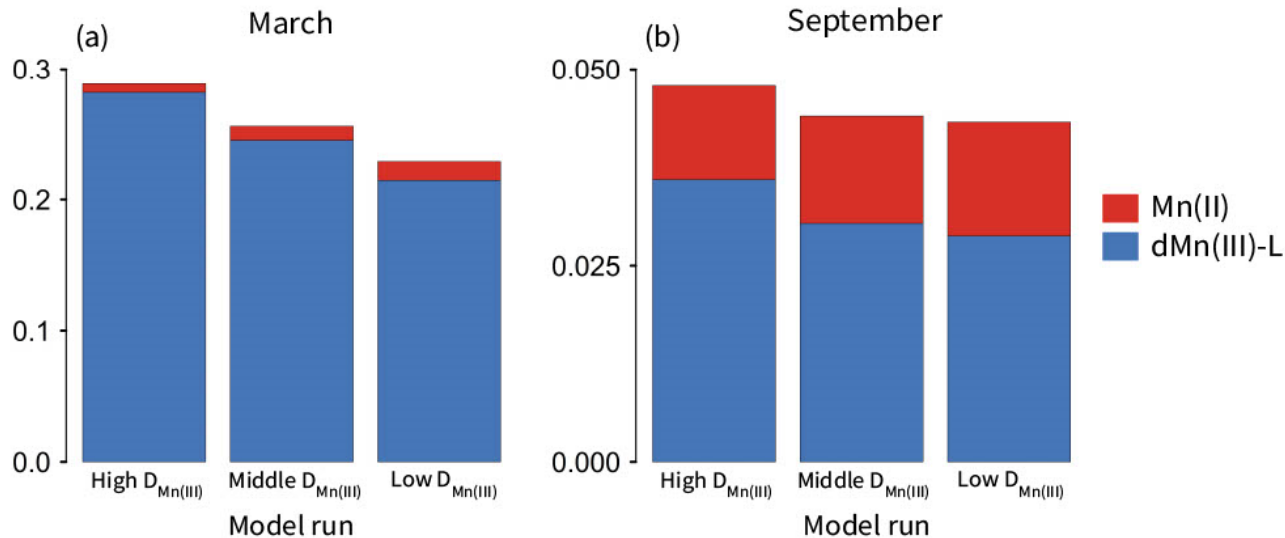


Figure S13: Variation in the benthic flux of dissolved Mn over the model runs with changing diffusion coefficient for $dMn(III)-L$ ($D_{Mn(III)}$) in March (A) and September (B). Note the different y-axes for the different months. The figure shows that a lower diffusion coefficient for $dMn(III)-L$ results in a lower benthic flux of total Mn and $dMn(III)-L$, but a slightly higher benthic flux of $Mn(II)$. The values for the high, middle and low $D_{Mn(III)}$ can be found in Table S6.

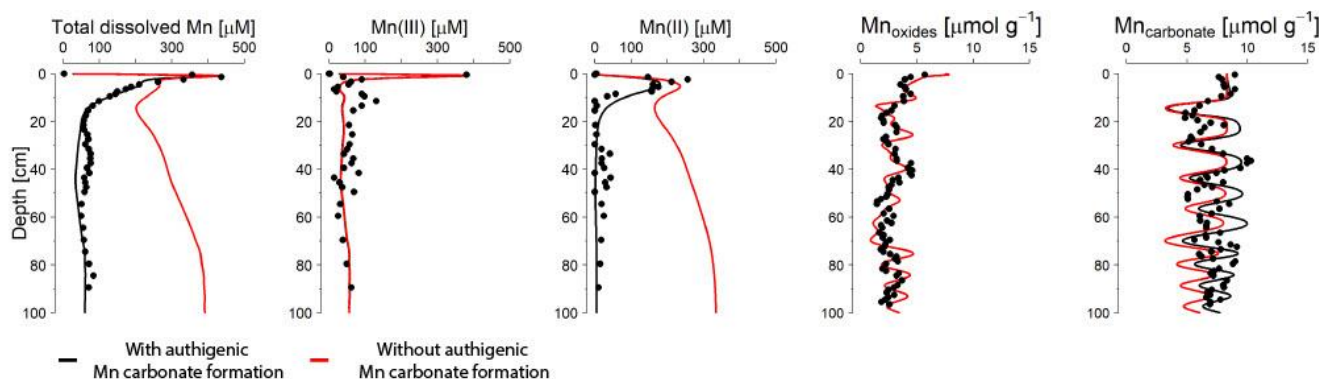


Figure S14: Model output when authigenic Mn carbonate precipitation is turned off in red versus the model base run in black. The difference in Mn carbonate concentrations between the model without Mn carbonate precipitation and the base run indicate the amount of Mn carbonate that, according to the model, has formed within the sediment.

S4. Tables

Table S1. Chemical species included in the model

Species	Notation
Solids	
Organic Matter ^a	OM ^{$\alpha/\beta/\gamma$}
Iron oxides ^a	Fe(OH) ₃ ^{$\alpha/\beta/\gamma$}
Iron monosulfide	FeS
Pyrite	FeS ₂
Elemental Sulfur	S ⁰
Siderite	FeCO ₃
Vivianite	Fe ₃ (PO ₄) ₂
Manganese oxide ^b	MnO ₂ ^{α/β}
Manganese carbonate	MnCO ₃
Solutes	
Chloride	Cl ⁻
Oxygen	O ₂
Nitrate	NO ₃ ⁻
Sulfate	SO ₄ ²⁻
Methane	CH ₄
Dissolved iron	Fe ²⁺
Ammonium ^c	ΣNH ₄ ⁺
Hydrogen sulfide ^c	ΣH ₂ S
Phosphate ^c	ΣH ₃ PO ₄
Dissolved Inorganic Carbon	DIC
Dissolved manganese (II)	Mn ²⁺
Dissolved manganese(III)-L	Mn ^{3+-L}

^a Consists of three types of species: reactive (α), less reactive (β) and non-reactive (γ)

^b Consists of two types of species: reactive (α) and less reactive (β)

^c Σ denotes that all species of an acid are included.

Table S2. Reaction pathways and stoichiometries implemented in the model

Primary redox reactions	
$OM^{\alpha,\beta} + a O_2 \rightarrow a CO_2 + b \Sigma NH_4^+ + c \Sigma H_3PO_4 + a H_2O$	R1
$OM^{\alpha,\beta} + 0.8 a NO_3 + 0.8 a H^+ \rightarrow a CO_2 + b \Sigma NH_4^+ + c \Sigma H_3PO_4 + 0.4 a N_2 + 1.4 a H_2O$	R2
$OM^{\alpha,\beta} + 4a MnO_2^a + 2 a H^+ \rightarrow 4a Mn^{3+} - L + a CO_2 + b \Sigma NH_4^+ + c \Sigma H_3PO_4 + 2 a H_2O$	R3
$OM^{\alpha,\beta} + 4a Fe(OH)_3^a + 4a \chi Fe_{ox}P + 12 a H^+ \rightarrow 4a Fe^{2+} + a CO_2 + b \Sigma NH_4^+ + (c + 4a \chi) \Sigma H_3PO_4 + 13a H_2O$	R4
$OM^{\alpha,\beta} + 0.5a SO_4^{2-} + a H^+ \rightarrow a CO_2 + b \Sigma NH_4^+ + c \Sigma H_3PO_4 + 0.5a \Sigma H_2S + a H_2O$	R5
$OM^{\alpha,\beta} \rightarrow 0.5a CO_2 + b \Sigma NH_4^+ + c \Sigma H_3PO_4 + 0.5a CH_4$	R6
Secondary and other reactions	
$O_2 + Fe^{2+} + 8 H_2O + 4 \chi \Sigma H_3PO_4 \rightarrow 4 Fe(OH)_3^a + 4 \chi Fe_{ox}P + 8 CO_2$	R7
$2 O_2 + FeS \rightarrow SO_4^{2-} + 2 Fe^{2+} + 4 H^+$	R8
$7 O_2 + 2 FeS_2 + 2 H_2O + 4 SO_4^{2-} \rightarrow 2 Fe^{2+} + 4 H^+$	R9
$2 O_2 + \Sigma H_2S + 2 HCO_3^- \rightarrow SO_4^{2-} + 2 CO_2 + 2 H_2O$	R10
$2 O_2 + CH_4 \rightarrow CO_2 + 2 H_2O$	R11
$2 Fe(OH)_3^a + 2 \chi Fe_{ox}P + H_2S + 4 CO_2 \rightarrow 2 Fe^{2+} + 2 \chi \Sigma H_3PO_4 + S^0 + 4 HCO_3^- + 2 H_2O$	R12
$Fe^{2+} + \Sigma H_2S \rightarrow FeS + 2 H^+$	R13
$FeS + \Sigma H_2S \rightarrow FeS_2 + H_2$	R14
$SO_4^{2-} + CH_4 + CO_2 \rightarrow 2 HCO_3^- + \Sigma H_2S$	R15
$CH_4 + 8 Fe(OH)_3^{a,\beta} + 8 \chi Fe_{ox}P + 15 H^+ \rightarrow HCO_3^- + 8 Fe^{2+} + 8 \chi \Sigma H_3PO_4 + 21 H_2O$	R16
$4 S^0 + 4 H_2O \rightarrow 3 \Sigma H_2S + SO_4^{2-} + 2 H^+$	R17
$FeS + S^0 \rightarrow FeS_2$	R18
$Fe(OH)_3^a + \chi Fe_{ox}P \rightarrow Fe(OH)_3^\beta + \chi \Sigma H_3PO_4$	R19
$2 Fe(OH)_3^\beta + 2 \chi Fe_{ox}P + \Sigma H_2S + 4 CO_2 \rightarrow 2 Fe^{2+} + 2 \chi \Sigma H_3PO_4 + S^0 + 4 HCO_3^- + 2 H_2O$	R20
$2 O_2 + \Sigma NH_4^+ + 2 HCO_3^- \rightarrow NO_3^- + 2 CO_2 + 3 H_2O$	R21
$3 Fe^{2+} + 2 \Sigma H_3PO_4 \rightarrow Fe_3(PO_4)_2 + 4 H^+$	R22
$Fe^{2+} + CO_3^{2-} \rightarrow FeCO_3$	R23
$FeCO_3 + \Sigma H_2S \rightarrow FeS + CO_2 + H_2O$	R24
$Fe_3(PO_4)_2 + 3 \Sigma H_2S \rightarrow 2 FeS + 2 \Sigma H_3PO_4 + 4 H^+$	R25
$Mn^{2+} + HCO_3^- + OH^- \rightarrow MnCO_3 + H_2O$	R26
$4 Mn^{2+} + O_2 + 4 H^+ + L \rightarrow 4 Mn^{3+} - L + 2 H_2O$	R27

$\text{MnO}_2^{a,\beta} + \text{Fe}^{2+} + \text{H}_2\text{O} + \text{H}^+ + \text{L} \rightarrow \text{Fe}(\text{OH})_3^a + \text{Mn}^{3+} - \text{L}$	R28
$\text{MnO}_2^a + \Sigma \text{H}_2\text{S} + 2 \text{H}^+ + \text{L} \rightarrow \text{S}^0 + \text{Mn}^{3+} - \text{L} + 2 \text{H}_2\text{O}$	R29
$\text{MnO}_2^a \rightarrow \text{MnO}_2^\beta$	R30
$\text{MnO}_2^\beta + \Sigma \text{H}_2\text{S} + 2 \text{H}^+ + \text{L} \rightarrow \text{S}^0 + \text{Mn}^{3+} - \text{L} + 2 \text{H}_2\text{O}$	R31
$4 \text{MnO}_2^{a,\beta} + \text{CH}_4 + 7 \text{H}^+ \rightarrow 4 \text{Mn}^{2+} + \text{HCO}_3^- + 5 \text{H}_2\text{O}$	R32
$4 \text{Mn}^{3+} - \text{L} + 2 \text{O}_2 + 4 \text{H}^+ \rightarrow 4 \text{MnO}_2^a + 2 \text{H}_2\text{O} + \text{L}$	R33
$\text{Mn}^{3+} - \text{L} + \Sigma \text{H}_2\text{S} \rightarrow \text{S}^0 + \text{Mn}^{2+} + \text{L}$	R34
$\text{Mn}^{3+} - \text{L} + \text{Fe}^{2+} + 3 \text{H}_2\text{O} \rightarrow \text{Mn}^{2+} + \text{Fe}(\text{OH})_3^a + 3 \text{H}^+ + \text{L}$	R35
$4 \text{Mn}^{3+} - \text{L} + \text{OM}^a + \text{H}_2\text{O} \rightarrow 4 \text{Mn}^{2+} + \text{CO}_2 + 3 \text{H}^+ + \text{L}$	R36

Organic matter is of the form $((\text{CH}_2\text{O})_a (\text{NH}_4^+)_b (\text{H}_3\text{PO}_4)_c)$, where $a=1$, $b= 1/15.45$ and $c = 106/1$. α , β , & γ describe different fractions (i.e. highly reactive, less reactive and refractory). χ describes the P:Fe ratios of $\text{Fe}(\text{OH})_3$ and has a value of 0.3 in the model.

160

Table S3. Reaction equations implemented in the model

Primary redox reaction equations	
$\text{R1} = k_{\alpha,\beta} \text{OM}^{\alpha,\beta} \left(\frac{[\text{O}_2]}{K_{m,\text{O}_2} + [\text{O}_2]} \right)$	E1
$\text{R2} = k_{\alpha,\beta} \text{OM}^{\alpha,\beta} \left(\frac{[\text{NO}_3^-]}{K_{m,\text{NO}_3^-} + [\text{NO}_3^-]} \right) \left(\frac{K_{m,\text{O}_2}}{K_{m,\text{O}_2} + [\text{O}_2]} \right)$	E2
$\text{R3} = k_{\alpha,\beta} \text{OM}^{\alpha,\beta} \left(\frac{[\text{MnO}_2]}{K_{m,\text{MnO}_2} + [\text{MnO}_2]} \right) \left(\frac{K_{m,\text{NO}_3^-}}{K_{m,\text{NO}_3^-} + [\text{NO}_3^-]} \right) \left(\frac{K_{m,\text{O}_2}}{K_{m,\text{O}_2} + [\text{O}_2]} \right)$	E3
$\text{R4} = k_{\alpha,\beta} \text{OM}^{\alpha,\beta} \left(\frac{[\text{Fe}(\text{OH})_3]}{K_{m,\text{Fe}(\text{OH})_3} + [\text{Fe}(\text{OH})_3]} \right) \left(\frac{K_{m,\text{MnO}_2}}{K_{m,\text{MnO}_2} + [\text{MnO}_2]} \right) \left(\frac{K_{m,\text{NO}_3^-}}{K_{m,\text{NO}_3^-} + [\text{NO}_3^-]} \right) \left(\frac{K_{m,\text{O}_2}}{K_{m,\text{O}_2} + [\text{O}_2]} \right)$	E4
$\text{R5} = k_{\alpha,\beta} \text{OM}^{\alpha,\beta} \left(\frac{[\text{SO}_4^{2-}]}{K_{m,\text{SO}_4^{2-}} + [\text{SO}_4^{2-}]} \right) \left(\frac{K_{m,\text{Fe}(\text{OH})_3}}{K_{m,\text{Fe}(\text{OH})_3} + [\text{Fe}(\text{OH})_3]} \right) \left(\frac{K_{m,\text{MnO}_2}}{K_{m,\text{MnO}_2} + [\text{MnO}_2]} \right) * \left(\frac{K_{m,\text{NO}_3^-}}{K_{m,\text{NO}_3^-} + [\text{NO}_3^-]} \right) \left(\frac{K_{m,\text{O}_2}}{K_{m,\text{O}_2} + [\text{O}_2]} \right)$	E5

$R6 = k_{\alpha,\beta} OM^{\alpha,\beta} \left(\frac{K_{m,SO_4^{2-}}}{K_{m,SO_4^{2-}} + [SO_4^{2-}]} \right) \left(\frac{K_{m,Fe(OH)_3}}{K_{m,Fe(OH)_3} + [Fe(OH)_3]} \right) \left(\frac{K_{m,MnO_2}}{K_{m,MnO_2} + [MnO_2]} \right) \\ * \left(\frac{K_{m,NO_3^-}}{K_{m,NO_3^-} + [NO_3^-]} \right) \left(\frac{K_{m,O_2}}{K_{m,O_2} + [O_2]} \right)$	E6
Secondary redox and other reaction equations	
$R7 = k_1 [O_2] [Fe^{2+}]$	E7
$R8 = k_2 [O_2] [FeS]$	E8
$R9 = k_3 [O_2] [FeS_2]$	E9
$R10 = k_4 [O_2] [\sum H_2S]$	E10
$R11 = k_5 [O_2] [CH_4]$	E11
$R12 = k_6 [Fe(OH)_3^{\alpha}] [\sum H_2S]$	E12
$R13 = k_7 [Fe^{2+}] [\sum H_2S]$	E13
$R14 = k_8 [FeS] [\sum H_2S]$	E14
$R15 = k_9 [SO_4^{2-}] [CH_4]$	E15
$R16 = k_{10} [Fe(OH)_3^{\alpha,\beta}] [CH_4]$	E16
$R17 = k_{11} [S^0]$	E17
$R18 = k_{12} [FeS] [S^0]$	E18
$R19 = k_{13} [Fe(OH)_3^{\alpha}]$	E19
$R20 = k_{14} [Fe(OH)_3^{\beta}] [\sum H_2S]$	E20
$R21 = k_{15} [O_2] [NH_4^+]$	E21
$R22 = k_{16} [Fe^{2+}] [HPO_4^{2-}]$	E22
$R23 = k_{17} [Fe^{2+}] [HCO_3^-]$	E23

$R24 = k_{18} [\text{FeCO}_3] [\sum \text{H}_2\text{S}]$	E24
$R25 = k_{19} [\text{Fe}_3(\text{PO}_4)_2] [\sum \text{H}_2\text{S}]$	E25
$R26 = k_{20} [\text{Mn}^{2+}] [\text{HCO}_3^-]$	E26
$R27 = k_{21} [\text{Mn}^{2+}] [\text{O}_2]$	E27
$R28 = k_{22} [\text{MnO}_2^{\alpha,\beta}] [\text{Fe}^{2+}]$	E28
$R29 = k_{23} [\text{MnO}_2^{\alpha}] [\sum \text{H}_2\text{S}]$	E29
$R30 = k_{24} [\text{MnO}_2^{\alpha}]$	E30
$R31 = k_{25} [\text{MnO}_2^{\beta}] [\sum \text{H}_2\text{S}]$	E31
$R32 = k_{26} [\text{MnO}_2^{\alpha,\beta}] [\text{CH}_4]$	E32
$R33 = k_{27} [\text{Mn}^{3+} - \text{L}] [\text{O}_2]$	E33
$R34 = k_{28} [\text{Mn}^{3+} - \text{L}] [\sum \text{H}_2\text{S}]$	E34
$R35 = k_{29} [\text{Mn}^{3+} - \text{L}] [\text{Fe}^{2+}]$	E35
$R36 = k_{30} [\text{Mn}^{3+} - \text{L}] [\text{OM}^{\alpha}]$	E36
$R37 = k_{31} [\text{OM}^{\alpha}]$	E37
$R38 = k_{32} [\text{NO}_3^-] [\text{CH}_4]$	E38
$R39 = k_{33} [\text{CO}_2] [\text{H}_2] \left(\frac{K_{m,\text{SO}_4^{2-}}}{K_{m,\text{SO}_4^{2-}} + [\text{SO}_4^{2-}]} \right) \left(\frac{K_{m,\text{Fe}(\text{OH})_3}}{K_{m,\text{Fe}(\text{OH})_3} + [\text{Fe}(\text{OH})_3]} \right) \left(\frac{K_{m,\text{MnO}_2}}{K_{m,\text{MnO}_2} + [\text{MnO}_2]} \right) *$ $\left(\frac{K_{m,\text{NO}_3^-}}{K_{m,\text{NO}_3^-} + [\text{NO}_3^-]} \right) \left(\frac{K_{m,\text{O}_2}}{K_{m,\text{O}_2} + [\text{O}_2]} \right)$	E39

Table S4. Reaction parameters used in the model

Parameter	Value	Unit	Source	Values in literature
k_{α}^*	1.62	yr ⁻¹	a, b	0.05 – 1.62
k_{β}^*	0.0086	yr ⁻¹	b, d	0.0025 - 0.0086

K_{O_2}	20	$\mu\text{mol L}^{-1}$	c	1 – 30
$K_{NO_3^-}$	20	$\mu\text{mol L}^{-1}$	c	4 – 80
K_{MnO_2}	32	$\mu\text{mol L}^{-1}$	c	4 – 32
$K_{Fe(OH)_3}$	65	$\mu\text{mol L}^{-1}$	c	65 – 100
$K_{SO_4^{2-}}$	1.6	$\mu\text{mol L}^{-1}$	c	1.6
k_1 (E7)	$1.4 \cdot 10^5$	mmol yr^{-1}	c	$1.4 \cdot 10^5$
k_2 (E8)	300	mmol yr^{-1}	c	300
k_3 (E9)	1	mmol yr^{-1}	c	1
k_4 (E10)	160	mmol yr^{-1}	c	160
k_5 (E11)	100	mmol yr^{-1}	c	107
k_6 (E12)	80	mmol yr^{-1}	c, g, i	8 - 100
k_7 (E13)	11840	mmol yr^{-1}	b, d	100 - 14800
k_8 (E14)	0.0003	mmol yr^{-1}	e, i	0.0003 – 0.0074
k_9 (E15)	1.344	mmol yr^{-1}	c, g	10 (c) – 120 (g)
k_{10} (E16)	$3.04 \cdot 10^{-6}$	mmol yr^{-1}	g, i	$1.6 \cdot 10^{-7}$ – 0.0074
k_{11} (E17)	3	yr^{-1}	f	3
k_{12} (E18)	0.1	mmol yr^{-1}	f, g	0.001 - 7
k_{13} (E19)	0.1	yr^{-1}		model constrained
k_{14} (E20)	0.444	mmol yr^{-1}	c, j	0.004 – 100
k_{15} (E21)	19500	mmol yr^{-1}	c, d	5000 – 39000
k_{16} (E22)	0.052	mmol yr^{-1}		model constrained
k_{17} (E23)	0.000351	mmol yr^{-1}	i	0.0027
k_{18} (E24)	0.0008	mmol yr^{-1}		model constrained
k_{19} (E25)	$8 \cdot 10^{-4}$	mmol yr^{-1}	i	$8 \cdot 10^{-4}$
k_{20} (E26)	0.05565	mmol yr^{-1}	k	0.265
k_{21} (E27)	15000	mmol yr^{-1}	c	800 - 20000
k_{22} (E28)	2.652	mmol yr^{-1}	f, k	0.002 - 2
k_{23} (E29)	1	mmol yr^{-1}	c	< 100000 (20)
k_{24} (E30)	1.8	yr^{-1}	f	1.8
k_{25} (E31)	0.02	mmol yr^{-1}	c	< 100000 (20)

k_{26} (E32)	0.000019	mmol yr ⁻¹	k	0.0017
k_{27} (E33)	144	mmol yr ⁻¹		model constrained
k_{28} (E34)	64	mmol yr ⁻¹		model constrained
k_{29} (E35)	0.025	mmol yr ⁻¹		model constrained
k_{30} (E36)	$2.5 \cdot 10^{-4}$	mmol yr ⁻¹		model constrained
k_{31} (E37)	0.15	yr ⁻¹		model constrained
k_{32} (E38)	0.5	mmol yr ⁻¹		model constrained
k_{33} (E39)	0.03675	yr ⁻¹		model constrained

165 a) Moodley et al. (2005); b) Reed et al. (2011a) c) Van Cappellen & Wang (1996); d) Reed et al. (2016); e) Rickard (1997);
f) Berg et al. (2003); g) Rooze et al. (2016); h) Egger et al. (2016a); i) Egger et al. (2016b); j) Lenstra et al. (2018)

*Following the approach of Reed et al. (2011b), we have assumed different reactivities of the organic matter towards the electron acceptors. The following factors have been used for the α fraction: O₂ = 1, NO₃ = 3, MnO₂ = 2.8, Fe(OH)₃ = 0.3, SO₄²⁻ = 1.7, methanogenesis = 0.5; for the β fraction the following factors have been used: O₂ = 1, NO₃⁻ = 3, MnO₂ = 1, Fe(OH)₃ = 0.3, SO₄²⁻ = 1, methanogenesis = 3.
170

Table S5. Environmental parameters used in the model. Values of porosity, temperature, salinity and the sedimentation rate are based on data for the study site.

Parameter	Symbol	Value	Unit
Porosity at surface	ϕ_0	0.944	vol/vol
Porosity at depth	ϕ_∞	0.888	vol/vol
Porosity e-folding distance	g	60	cm
Sediment density	r	2.65	g cm ⁻³
Temperature	T	8.4	°C
Salinity	S	35	-
Pressure	P	5.5	bar
Tortuosity	q^2	$1 - 2\ln(\phi)$	-
Molecular diffusion coefficient corrected for tortuosity	D'	$D' = \frac{D_m}{\theta^2}$	cm ² yr ⁻¹
Sediment accumulation rate**	F_{Sed}	**	g cm ⁻² yr ⁻¹

Advective velocity at surface	n_0	$\frac{F_{sed}}{\rho(1 - \varphi_0)}$	cm yr ⁻¹
Advective velocity at depth	n_∞	$\frac{F_{sed}}{\rho(1 - \varphi_\infty)}$	cm yr ⁻¹
** Sedimentation rate variations over the years			
Year	December – July	July - December	Unit
0 – 60	2.97	2.97	g cm ⁻² yr ⁻¹
60 – 75	0.69	3.93	g cm ⁻² yr ⁻¹
75 – 80	3.93	2.00	g cm ⁻² yr ⁻¹

175 **Table S6. The various diffusion coefficients used for Mn(III) ($D_{Mn(III)}$) to evaluate the effect of the choice of the diffusion coefficient for Mn(III) when it forms a complex with an organic ligand.**

Name	Scenario	Value	Range in literature	Sources
High $D_{Mn(III)}$	$DMn(III) = DMn(II)$ As calculated by reactran package	132.6 cm ² yr ⁻¹	-	<i>a</i>
Middle $D_{Mn(III)}$	$DMn(III)$ is within the range of diffusion coefficients for dissolved organic matter	33.1 cm ² yr ⁻¹	22.7 – 81 cm ² yr ⁻¹	<i>b, c</i>
Low $D_{Mn(III)}$	$DMn(III)$ is constrained by the model, by fitting Mn(III) to the collected data. This is the $DMn(III)$ that is used in the model throughout the paper.	16.6 cm ² yr ⁻¹	-	

Sources: *a*) Soetaert & Meysman (2012); *b*) Burdige et al. (1999); *c*) Burdige et al. (2004)

Table S7. Boundary conditions of solids and solutes at the sediment-water interface in the model. For the time-dependent fluxes of $OM^{\alpha,\beta,\gamma}$, $Fe(OH)_3^{\alpha,\beta,\gamma}$, $MnO_2^{\alpha,\beta}$ and $MnCO_3$ and concentration of O_2 the minimum and maximum fluxes and concentrations are given. For all chemical species, a zero-gradient boundary condition was specified at the bottom of the model domain.

Solids	Flux at sediment-water interface		Unit
FeS	0.4 * 10 ⁻⁴		mol m ⁻² yr ⁻¹
FeS ₂	0		mol m ⁻² yr ⁻¹
S ⁰	0		mol m ⁻² yr ⁻¹
FeCO ₃	2		mol m ⁻² yr ⁻¹
Fe ₃ (PO ₄) ₂	0		mol m ⁻² yr ⁻¹
	Min	Max	
OM ^α	9.51	52.31	mol m ⁻² yr ⁻¹
OM ^β	45.36	72.58	mol m ⁻² yr ⁻¹
OM ^γ	0.001	0.001	mol m ⁻² yr ⁻¹
Fe(OH) ₃ ^α	0.0028	6.44	mol m ⁻² yr ⁻¹
Fe(OH) ₃ ^β	3.28	4.68	mol m ⁻² yr ⁻¹
Fe(OH) ₃ ^γ	0	0	mol m ⁻² yr ⁻¹
MnO ₂ ^α	0.0108	0.081	mol m ⁻² yr ⁻¹
MnO ₂ ^β	0.0235	0.216	mol m ⁻² yr ⁻¹
MnCO ₃	0.0624	0.163	mol m ⁻² yr ⁻¹
Solutes	Bottom water concentrations		Unit
	Min	Max	
O ₂	0	0.205	mmol L ⁻¹
ΣH ₂ S	0	0.111	mmol L ⁻¹
Cl ⁻	532		mmol L ⁻¹
NO ₃ ⁻	0		mmol L ⁻¹
SO ₄ ²⁻	27.49		mmol L ⁻¹
CH ₄	0		mmol L ⁻¹
Fe ²⁺	0		mmol L ⁻¹
ΣNH ₄ ⁺	0		mmol L ⁻¹

$\Sigma\text{H}_3\text{PO}_4$	0	mmol L^{-1}
DIC	3	mmol L^{-1}
Mn^{2+}	0	mmol L^{-1}
Mn^{3+}	0	mmol L^{-1}

References

- 190 Berg, P., Rysgaard, S., & Thamdrup, B. O. : Dynamic Modeling of Early Diagenesis and Nutrient Cycling. A Case Study in an Arctic Marine Sediment. *Am. J. Sci.*, 303, 905–955, 2003.
- Boudreau, B. P.: Diagenetic models and their implementation : modelling transport and reactions in aquatic sediments *Modelling Transport and Reactions in Aquatic Sediments*. Springer Berlin Heidelberg. <https://doi.org/10.1007/978-3-642-60421-8>, 1997.
- 195 Boudreau, P.: A Method-of-Lines Code For Carbon and Nutrient Diagenesis in Aquatic Sediments. *Comput. Geosci.*, 22(5), 479–496, 1996.
- Burdige, D. J., Berelson, W. M., Coale, K. H., McManus, J., & Johnson, K. S.: Fluxes of dissolved organic carbon from California continental margin sediments. *Geochim. Cosmochim. Ac.*, 63(10), 1507–1515, 1999.
- Burdige, D. J., Kline, S. W., & Chen, W.: Fluorescent dissolved organic matter in marine sediment pore waters. *Mar. Chem.*, 89, 289–311. <https://doi.org/10.1016/j.marchem.2004.02.015>, 2004.
- 200 Cline, J. D.: Spectrophotometric Determination of Hydrogen Sulfide in Natural Waters. *Limnol. Oceanogr.*, 14(3), 454–458. <https://doi.org/10.4319/lo.1969.14.3.0454>, 1969.
- Egger, M., Kraal, P., Jilbert, T., Sulu-gambari, F., Sapart, C. J., & Röckmann, T.: Anaerobic oxidation of methane alters sediment records of sulfur , iron and phosphorus in the Black Sea. *Biogeosciences*, 5333–5355. <https://doi.org/10.5194/bg-13-5333-2016>, 2016.
- 205 Egger, M., Lenstra, W., Jong, D., Meysman, F. J. R., Sapart, C. J., Van Der Veen, C., Röckmann, T., Gonzalez, S., & Slomp, C. P.: Rapid sediment accumulation results in high methane effluxes from coastal sediments. *PLoS ONE*, 11(8), 1–22. <https://doi.org/10.1371/journal.pone.0161609>, 2016.
- 210 Froelich, P. N., Klinkhammer, G. P., Bender, M. L., Luedtke, N. A., Heath, G. R., Cullen, D., Dauphin, P., Hammond, D., & Hartman, B.: Early oxidation of organic matter in pelagic sediments of the eastern equatorial Atlantic : suboxic diagenesis. *Geochim. Cosmochim. Ac.*, 43, 1075–1090, 1979.
- Hagens, M., Slomp, C. P., Meysman, F. J. R., Seitaj, D., Harlay, J., Borges, A. V., & Middelburg, J. J.: Biogeochemical processes and buffering capacity concurrently affect acidification in a seasonally hypoxic coastal marine basin. *Biogeosciences*, 12(5), 1561–1583. <https://doi.org/10.5194/bg-12-1561-2015>, 2015.
- 215 Hulth, S., Aller, R. C., & Gilbert, F.: Coupled anoxic nitrification / manganese reduction in marine sediments. *Geochim. Cosmochim. Ac.*, 63(1), 49–66, 1999.
- Karolewski, J. S., Sutherland, K. M., Hansel, C. M., & Wankel, S. D.: An isotopic study of abiotic nitrite oxidation by ligand-bound manganese (III). *Geochim. Cosmochim. Ac.*, 293, 365–378. <https://doi.org/10.1016/j.gca.2020.11.004>, 2021.
- Lenstra, W. K., Egger, M., Helmond, N. A. G. M. Van, Kritzberg, E., Conley, D. J. & Slomp, C.P.: Large variations in iron input to an oligotrophic Baltic Sea estuary : impact on sedimentary phosphorus burial. *Biogeosciences*, 6979–6996, 2018.
- 220 Lenstra, W. K., Klomp, R., Molema, F., Behrends, T., & Slomp, C. P.: A sequential extraction procedure for particulate manganese and its application to coastal marine sediments. *Chem. Geol.*, 584(June), 120538. <https://doi.org/10.1016/j.chemgeo.2021.120538>, 2021.
- Meysman, F. J. R., Boudreau, B. P., & Middelburg, J. J.: Modeling reactive transport in sediments subject to bioturbation and compaction. *Geochim. Cosmochim. Ac.*, 69(14), 3601–3617. <https://doi.org/10.1016/j.gca.2005.01.004>, 2005.

- 225 Moodley, L., Middelburg, J. J., Herman, P. M. J., Soetaert, K., & de Lange, G. J.: Oxygenation and organic-matter preservation in marine sediments : Direct experimental evidence from ancient organic carbon – rich deposits. *Geology*, 11, 889–892. <https://doi.org/10.1130/G21731.1>, 2005.
- Reed, D. C., Gustafsson, B. G., & Slomp, C. P.: Shelf-to-basin iron shuttling enhances vivianite formation in deep Baltic Sea sediments. *Earth and Planetary Science Letters*, 434, 241–251. <https://doi.org/10.1016/j.epsl.2015.11.033>, 2016.
- 230 Reed, D. C., Slomp, C. P., & de Lange, G. J.: A quantitative reconstruction of organic matter and nutrient diagenesis in Mediterranean Sea sediments over the Holocene. *Geochim. Cosmochim. Ac.*, 75(19), 5540–5558. <https://doi.org/10.1016/j.gca.2011.07.002>, 2011a.
- Reed, D. C., Slomp, C. P., & Gustafsson, B. G.: Sedimentary phosphorus dynamics and the evolution of bottom-water hypoxia: A coupled benthic-pelagic model of a coastal system. *Limnol. Oceanogr.*, 56(3), 1075–1092. <https://doi.org/10.4319/lo.2011.56.3.1075>, 2011b.
- 235 Rickard, D.: Kinetics of pyrite formation by the H₂S oxidation of iron (II) monosulfide in aqueous solutions between 25 and 125 ° C : The rate equation. *Geochim. Cosmochim. Ac.*, 61(1), 115–134, 1997.
- Rooze, J., Egger, M., Tsandev, I., & Slomp, C. P.: Iron-dependent anaerobic oxidation of methane in coastal surface sediments: Potential controls and impact. *Limnol. Oceanogr.*, 61(1), S267–S282. <https://doi.org/10.1002/lno.10275>, 2016.
- 240 Soetaert, K., & Meysman, F.: Environmental Modelling & Software Reactive transport in aquatic ecosystems : Rapid model prototyping in the open source software R. *Environ. Model. Softw.*, 32, 49–60. <https://doi.org/10.1016/j.envsoft.2011.08.011>, 2012.
- Solórzano, L.: Determination of Ammonia in Natural Waters by the Phenolhypochlorite Method. *Limnol. Oceanogr.*, 14(September), 799–801. <https://doi.org/10.4319/lo.1969.14.5.0799>, 1968.
- 245 Thamdrup, B., & Dalsgaard, T.: The fate of ammonium in anoxic manganese oxide-rich marine sediment. *Geochim. Cosmochim. Ac.*, 64(24), 4157–4164, 2000.
- Van Cappellen, P., & Wang, Y.: Cycling of iron and manganese in surface sediments: a general theory for the coupled transport and reaction of carbon, oxygen, nitrogen, sulfur, iron and manganese. *Am J Sci*, 296(March), 197–243, 1996.
- 250 Żygadłowska, O. M., Venetz, J., Klomp, R., Lenstra, W. K., Van Helmond, N. A. G. M., Röckmann, T., Wallenius, A. J., Dalcin Martins, P., Veraart, A. J., Jetten, M. S. M., & Slomp, C. P.: Pathways of methane removal in the sediment and water column of a seasonally anoxic eutrophic marine basin. *Front Mar. Sci.*, January, 1–15. <https://doi.org/10.3389/fmars.2023.1085728>, 2023.
- Żygadłowska, O. M., van Helmond, N. A. G. M., Lenstra, W. K., Klomp, R., Accou, R., Puyk, R., Dickson, A. J., Jetten, M. S. M., & Slomp, C. P.: Seasonal euxinia in a coastal basin: Impact on sedimentary molybdenum enrichments and isotope signatures. *Chem. Geol.*, 670(September), 122297. <https://doi.org/10.1016/j.chemgeo.2024.122297>, 2024a.
- 255 Żygadłowska, O. M., Venetz, J., Lenstra, W. K., Van Helmond, N. A. G. M., Klomp, R., Röckmann, T., & Slomp, C. P.: Ebullition drives high methane emissions from a eutrophic coastal basin. *Geochim. Cosmochim. Ac.*, 384, 1–13. <https://doi.org/10.1016/j.gca.2024.08.028>, 2024b.